

Dual-function terahertz metasurface based on vanadium dioxide and graphene

Jiu-Sheng Li(李九生) and Zhe-Wen Li(黎哲文)

Citation: Chin. Phys. B, 2022, 31 (**9**): 094201. DOI: 10.1088/1674-1056/ac5884
Journal homepage: http://cpb.iphy.ac.cn; http://iopscience.iop.org/cpb

What follows is a list of articles you may be interested in

Design of an all-dielectric long-wave infrared wide-angle metalens

Ning Zhang(张宁), Qingzhi Li(李青芝), Jun Chen(陈骏), Feng Tang(唐烽),Jingjun Wu(伍景军), Xin Ye(叶鑫), and Liming Yang(杨李茗)
Chin. Phys. B, 2022, 31 (**7**): 074212. DOI: 10.1088/1674-1056/ac4026

Multi-function terahertz wave manipulation utilizing Fourier convolution operation metasurface

Min Zhong(仲敏) and Jiu-Sheng Li(李九生)
Chin. Phys. B, 2022, 31 (**5**): 054207. DOI: 10.1088/1674-1056/ac46c0

An ultra-wideband 2-bit coding metasurface using Pancharatnam—Berry phase for radar cross-section reduction

Bao-Qin Lin(林宝勤), Wen-Zhun Huang(黄文准), Lin-Tao Lv(吕林涛), Jian-Xin Guo(郭建新),Yan-Wen Wang(王衍文), and Hong-Jun Ye(叶红军)
Chin. Phys. B, 2022, 31 (**3**): 034204. DOI: 10.1088/1674-1056/ac11ec

Wideband switchable dual-functional terahertz polarization converter based on vanadium dioxide-assisted metasurface

De-Xian Yan(严德贤), Qin-Yin Feng(封覃银), Zi-Wei Yuan(袁紫微), Miao Meng(孟淼), Xiang-Jun Li(李向军), Guo-Hua Qiu(裘国华), and Ji-Ning Li(李吉宁)
Chin. Phys. B, 2022, 31 (**1**): 014211. DOI: 10.1088/1674-1056/ac05a7

Solar energy full-spectrum perfect absorption and efficient photo-thermal generation

Zhefu Liao(廖喆夫), Zhengqi Liu(刘正奇), Qizhao Wu(吴起兆), Xiaoshan Liu(刘晓山), Xuefeng Zhan(詹学峰), Gaorong Zeng(曾高荣), and Guiqiang Liu(刘桂强)
Chin. Phys. B, 2021, 30 (**8**): 084206. DOI: 10.1088/1674-1056/ac0696

Dual-function terahertz metasurface based on vanadium dioxide and graphene

Jiu-Sheng Li(李九生)† and Zhe-Wen Li(黎哲文)

Centre for THz Research, China Jiliang University, Hangzhou 310018, China

(Received 8 October 2021; revised manuscript received 24 January 2022; accepted manuscript online 25 February 2022)

A dual-function terahertz metasurface based on VO_2 and graphene is proposed in this paper. It consists of a gold layer embedded with VO_2 patches, a SiO_2 spacer layer, a VO_2 layer, graphene and a SiO_2 spacer substrate. When the bottom VO_2 layer is in the metallic state, the designed metasurface can achieve absorption. When the top VO_2 patches are in the metallic state, the proposed metasurface can be used as a single-band absorber with terahertz absorptance of 99.7% at 0.736 THz. When the top VO_2 patches are in the insulating state, the designed structure behaves as a dual-band absorber with an absorptance of 98.9% at 0.894 THz and 99.9% at 1.408 THz. In addition, the absorber is polarization insensitive and keeps good performance at large angles of incidence. When the bottom VO_2 is in an insulating state, the metasurface shows electromagnetically induced transparency. The transparent window can be dynamically regulated by controlling the chemical potential of graphene. The proposed metasurface exhibits the advantages of terahertz absorption, electromagnetically induced transparency and dynamic control, which provides more options for the design of terahertz devices in the future.

Keywords: metasurface, switchable terahertz absorber, electromagnetically induced transparency

PACS: 42.25.Bs, 42.50.Gy, 78.20.Bh **DOI:** 10.1088/1674-1056/ac5884

1. Introduction

Vanadium dioxide (VO_2) and graphene have attracted much attention due to their excellent external control properties. VO_2 can switch to different phase transition states as the temperature changes.[1,2] Moreover, the phase transition process can be accomplished by thermal,[3,4] electrical[5,6] or optical control.[7] When working at room temperature, the lattice structure of VO_2 is monoclinic (the insulating state). When the temperature reaches 68 °C, the lattice of VO_2 is distorted into a tetragonal structure (the metallic state). This state is reversible, and the electromagnetic properties of VO_2 will change significantly during this process.[8] In the terahertz region, VO_2 is usually embedded in a metasurface to achieve dynamic regulation. In 2019, Liu *et al.*[9] proposed an adjustable absorber based on VO_2. With a change in the phase transition state, the absorber is converted from low absorption to broadband high absorption. When the temperature exceeds 70 °C, the absorption bandwidth reaches 2 THz. In 2020, Dong *et al.*[10] proposed a chiral metasurface composed of hybrid gold–VO_2 structures, and realized the switching on or off of asymmetric transmission by adjusting the phase of VO_2 from the insulating state to the metallic state and vice versa. Based on the transition of VO_2, Deng *et al.*[11] investigated a switchable metamaterial. Their device behaves as a cross converter when the VO_2 is metallic, while it behaves as an analog with electromagnetically induced transparency when VO_2 is switched to the insulating state.

Graphene is composed of carbon atoms in a planar hexagonal lattice. As a two-dimensional monolayer material,[12] a graphene surface can excite surface plasmons from the mid-infrared to terahertz bands. Compared with traditional metals, graphene has fewer free charges, and its free charge concentration can be changed by chemical doping or a bias voltage. Hence, the conductivity of graphene can be manipulated by changing the chemical potential. In 2019, Xiang *et al.*[13] investigated a tunable dual-band perfect absorber based on graphene. With an increase in the Fermi energy, the amplitude and frequency band of the absorption peak could be controlled. In 2020, Sun *et al.*[14] proposed a novel multifunctional device based on a hybrid metal–graphene metamaterial with electromagnetically induced transparency in the terahertz band. An ultra-broadband transmission window with a bandwidth of 1.23 THz can be obtained and the spectral extinction ratio can be tuned from 26% to 98% by changing the Fermi level of graphene. Moreover, metasurfaces based on VO_2 and graphene are increasingly being reported in the literature. In 2020, Zhu *et al.*[15] presented a switchable and tunable terahertz absorber based on the Fermi energy level of graphene and the phase transition properties of VO_2. When VO_2 is in the insulating state, broadband absorption properties are achieved. When VO_2 is in the metallic state, the device acts as a tunable multi-band absorber. In 2021, Liu *et al.*[16] proposed a bifunctional metamaterial which can realize a dynamic switch between beam steering and broadband absorption as the phase state of the VO_2 changes. By changing the Fermi energy level of graphene, the incident wave is scattered in different patterns

†Corresponding author. E-mail: lijsh@cjlu.edu.cn

© 2022 Chinese Physical Society and IOP Publishing Ltd

and the absorptance can also be gradually changed.

In this paper, we design a dual-function terahertz metasurface by utilizing the dynamic properties of graphene and VO_2. When the bottom VO_2 is in the metallic state, the metasurface can be switched between a single-band and dual-band absorber under different states of the top VO_2 patches (i.e., when the top VO_2 is in the metallic state, the designed metasurface behaves as a single-band absorber with an absorptance of 99.7% at 0.736 THz and when the top VO_2 is in the insulating state, the proposed metasurface acts as a dual-band absorber with an absorptance of 98.9% at 0.894 THz and 99.9% at 1.408 THz). When the bottom VO_2 is in the insulating state, the metasurface achieves electromagnetically induced transparency (EIT), and dynamic control of the transparency window and group delay can be manifested by changing the chemical potential of graphene. The designed metasurface shows the advantages of function switching and dynamic control.

2. Structure design

Figure 1 shows a three-dimensional (3D) structure diagram of the multifunctional terahertz metasurface, which consists of a gold pattern layer, a SiO_2 layer, a VO_2 layer, graphene and a SiO_2 bottom spacer substrate. The gold pattern is composed of four split rings and a cross. The gap is embedded with eight VO_2 patches. The optimized structure parameters are as follows: $P = 120$ μm, $l = 20$ μm, $a = 32$ μm, $s = 8$ μm, $w = 8$ μm, $g_1 = 8$ μm, and $g_2 = 21.2$ μm (the symbols are defined in Fig. 1). The thicknesses of the gold layer, SiO_2 spacer substrate, VO_2 film layer, graphene film layer and SiO_2 bottom spacer substrate are 0.5 μm, 7.5 μm, 1 μm, 0.01 μm, and 3 μm, respectively. Numerical simulations were performed using the finite difference frequency domain solver of CST Microwave Studio, for which the unit cell boundary conditions were set along the x- and y-directions, and the open boundary conditions were applied in the z-direction.

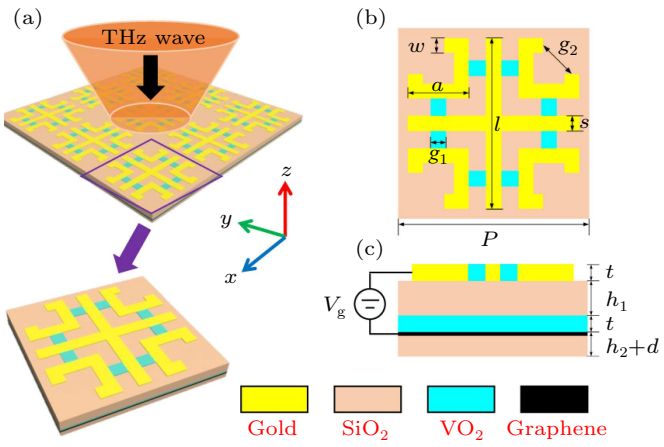


Fig. 1. (a) The 3D structure diagram of the proposed metasurface. (b) Top view of the unit cell. (c) Side view of the unit cell.

In the terahertz regime, the dielectric function of VO_2 can be given by the Drude model[17]

$$\varepsilon(\omega) = \varepsilon_\infty - \frac{\omega_p^2(\sigma)}{\omega^2 + i\gamma\omega}, \tag{1}$$

where $\varepsilon_\infty = 12$ is the dielectric permittivity at infinite frequency and $\gamma = 5.75 \times 10^{13}$ rad·s^{-1} is the collision frequency. The plasma frequency ω_p can be approximately defined as

$$\omega_p^2(\sigma) = \frac{\sigma}{\sigma_{ref}}\omega_p^2(\sigma_{ref}), \tag{2}$$

where $\sigma_{ref} = 3.0 \times 10^5$ S·m^{-1} and $\omega_p(\sigma_{ref}) = 1.4 \times 10^{15}$ rad·s^{-1}. In addition, the surface conductivity of graphene $\sigma(\omega, \mu_c, \Gamma, T)$ can be calculated by the Kubo formula[18,19]

$$\begin{aligned}\sigma(\omega,\mu_c,\Gamma,T) &= \frac{ie^2(\omega - i\Gamma)}{\pi\hbar^2} \\ &\times \frac{1}{(\omega - i\Gamma)^2}\int_0^\infty \left(\frac{\partial f_d(\varepsilon)}{\partial\varepsilon} - \frac{\partial f_d(-\varepsilon)}{\partial\varepsilon}\right)\varepsilon\,d\varepsilon \\ &- \int_0^\infty \frac{f_d(\varepsilon) - f_d(-\varepsilon)}{(\omega - i\Gamma)^2 - 4(\varepsilon/\hbar)^2}\,d\varepsilon, \end{aligned} \tag{3}$$

$$f_d(\varepsilon) = (e^{(\varepsilon-\mu_c)/(k_B T)} + 1)^{-1}, \tag{4}$$

where e is the electron charge, ω is the angular frequency, $\hbar = h/2\pi$ represents the reduced Planck's constant, T is the temperature, ε is the energy, $f_d(\varepsilon)$ represents the Fermi–Dirac distribution, k_B is the Boltzmann constant, μ_c is the chemical potential, Γ is the phenomenological scattering rate and $2\Gamma = \tau^{-1}$, τ is the relaxation time. When $k_B T \ll |\mu_c|$, formula (3) can be expressed as

$$\sigma(\omega,\mu_c,\Gamma,T) = \sigma_{intra} + \sigma_{inter}, \tag{5}$$

where σ_{intra} is the in-band conductivity and σ_{inter} is the inter-band conductivity, which are calculated by

$$\sigma_{intra} = i\frac{e^2 k_B T}{\pi\hbar^2(\omega - i\Gamma)}\left(\frac{\mu_c}{k_B T} + 2\ln(e^{-\mu_c/(k_B T)} + 1)\right), \tag{6}$$

$$\sigma_{inter} = \frac{ie^2}{4\pi\hbar}\ln\left(\frac{2|\mu_c| - (\omega - i\Gamma)\hbar}{2|\mu_c| + (\omega - i\Gamma)\hbar}\right). \tag{7}$$

3. Results analysis

3.1. Switching between single- and dual-band absorption

The absorptance of the proposed metasurface is written as follows:

$$A = 1 - R - T = 1 - |S_{11}|^2 - |S_{21}|^2, \tag{8}$$

where R and T represent reflectance and transmittance, respectively, while S_{11} and S_{21} represent reflection and transmission parameters, respectively. Figure 2(a) shows the different states of the absorption curve of the top VO_2 patch through phase transition while the bottom VO_2 film is in the metallic state. When the top VO_2 patches are in the insulating state,

the metasurface behaves as a dual-band absorber, and the absorptances at 0.894 THz and 1.408 THz are 98.9% and 99.9%, respectively. When the temperature rises to 68 °C, the bottom VO_2 film becomes metallic, and the designed structure is converted to a single-band absorber with an absorptance of 99.7% at 0.736 THz. The impedance matching theory[20] is introduced to analyze the structure, as follows:

$$Z = \sqrt{\frac{(1+S_{11})^2 - S_{21}^2}{(1-S_{11})^2 - S_{21}^2}} = \frac{Z_1}{Z_0}, \tag{9}$$

where Z_1 represents the equivalent surface impedance of the proposed device and Z_0 is the free space impedance. When the effective impedance matches the free space impedance, the relative impedance Z is close to 1, which realizes perfect absorption. The real and imaginary parts of the relative impedance of the designed metasurface are shown in Figs. 2(b) and 2(c). At 0.894 THz, the real and imaginary parts of the impedance are of 0.845 and 0.111, respectively. At 1.408 THz, the real and imaginary parts of the impedance are 1.035 and 0.034, respectively. Moreover, the real and imaginary parts of the impedance are 1.099 and −0.028, respectively, at 0.736 THz. This indicates that the designed structure has low reflectivity and high absorptance at the three frequencies. From Fig. 2(a), one can see that the perfect absorption is close to 100%. In addition, due to its symmetrical structure, the designed structure is polarization insensitive and can achieve the same absorption effect regardless of the incident waves being TE or TM.

In order to introduce the absorption mechanism at different frequencies, figure 3 illustrates the electric field distribution at the top and bottom of the switchable absorber at different resonant frequencies. One can see from Figs. 3(a) and 3(b) that pairs of induced charges gather at the top and bottom layers of the metasurface pattern, which indicates a dipole excited on the metal and VO_2 layer. At the same time, the direction of flow of charge in the VO_2 layer is opposite to that in the top metal layer. Therefore, the strong coupling between the two layers leads to magnetic resonance, and the electric and magnetic dipole resonances give rise to a perfect absorption peak at 0.736 THz. Similarly, figures 3(c) and 3(d) display that the top charges are mainly concentrated at the crossing ends, and the direction of charge flow is opposite to that of the bottom VO_2 layer. The absorption peak at 0.894 THz is also caused by the electric dipole resonance and magnetic dipole resonance. In Figs. 3(e) and 3(f), the result show that the positive and negative charges are mainly concentrated at the two ends of the four split rings, and four dipole-like pairs are accumulated. The electric octopoles between the top and bottom layers can be clearly observed; these are opposite to each other. Due to the strong interaction of the electric octopole mode, a four-harmonic magnetic resonance is formed.

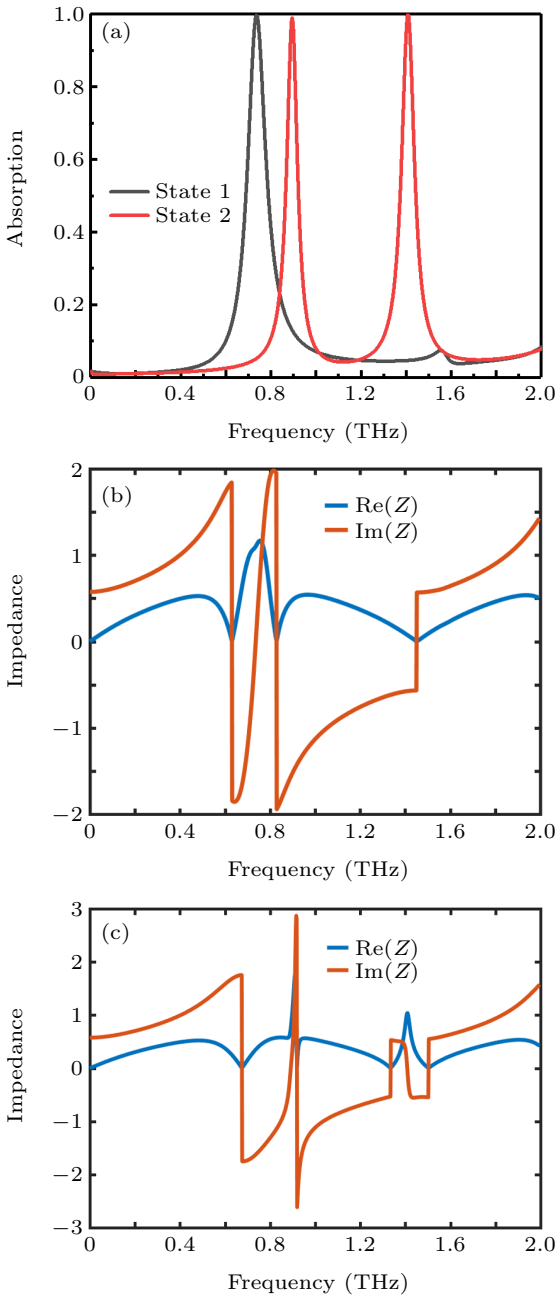


Fig. 2. (a) Absorption curves of VO_2 in the metallic and insulating states. (b) Real and imaginary parts of the impedance of a single-band absorber. (c) Real and imaginary parts of the impedance of a dual-band absorber.

We also studied the relationship between absorption and the terahertz wave angle. Figures 4(a) and 4(d) show the absorption spectra with different polarization angles for single-band and dual-band absorbers with vertically incident terahertz waves. When the polarization angle changes from 0° to 90° , the terahertz absorption spectra reveal polarization-insensitive characteristics, caused by the symmetry of the structure. Figures 4(b) and 4(c) show the absorption spectra of the single-band absorbers with the angle of incidence changing under TE and TM modes. For the TE mode, the angle of incidence varies from 0° to 60°, and the absorptance remains

above 0.8. The peak absorption rate decreases with increasing angle of incidence. That is to say, the direction of the electric field changes with the angle of incidence, which results in a decrease in the intensity of electric resonance. For the TM mode, the electric field does not change direction. In this case, when the angle of incidence is 70°, the absorption peak also maintains a high absorption rate above 0.9. It is worth noting that when the angle of incidence is above 40°, some undesirable absorption peaks appear in the absorption spectrum. This is because with an increase in the angle of incidence some parasitic resonances in the metasurface increase sharply. Figures 4(e) and 4(f) display the absorption spectra of the dual-band absorber with change in the angle of incidence for TE and TM modes. For the TE mode, when the angle of incidence varies from 0° to 40°, the two absorption peaks are above 0.8. In particular, the first absorption peak can remain at 0.9 when the angle of incidence reaches 70°. For the TM mode, when the angle of incidence is 60°, the two absorption peaks remain above 0.9. Similarly, absorption peaks caused by high resonance modes can be observed in the TM mode. This confirms that when the designed metasurface is used as switchable absorber it is insensitive to the polarization angle and can still maintain high absorption under a large angle of incidence.

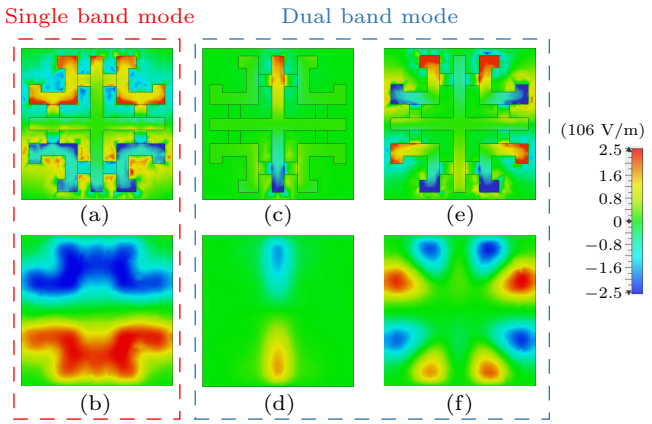


Fig. 3. Electric field distribution: at the top layer at 0.736 THz (a), 0.894 THz (c) and 1.408 THz (e) and at the bottom layer at 0.736 THz (b), 0.894 THz (d) and 1.408 THz (f).

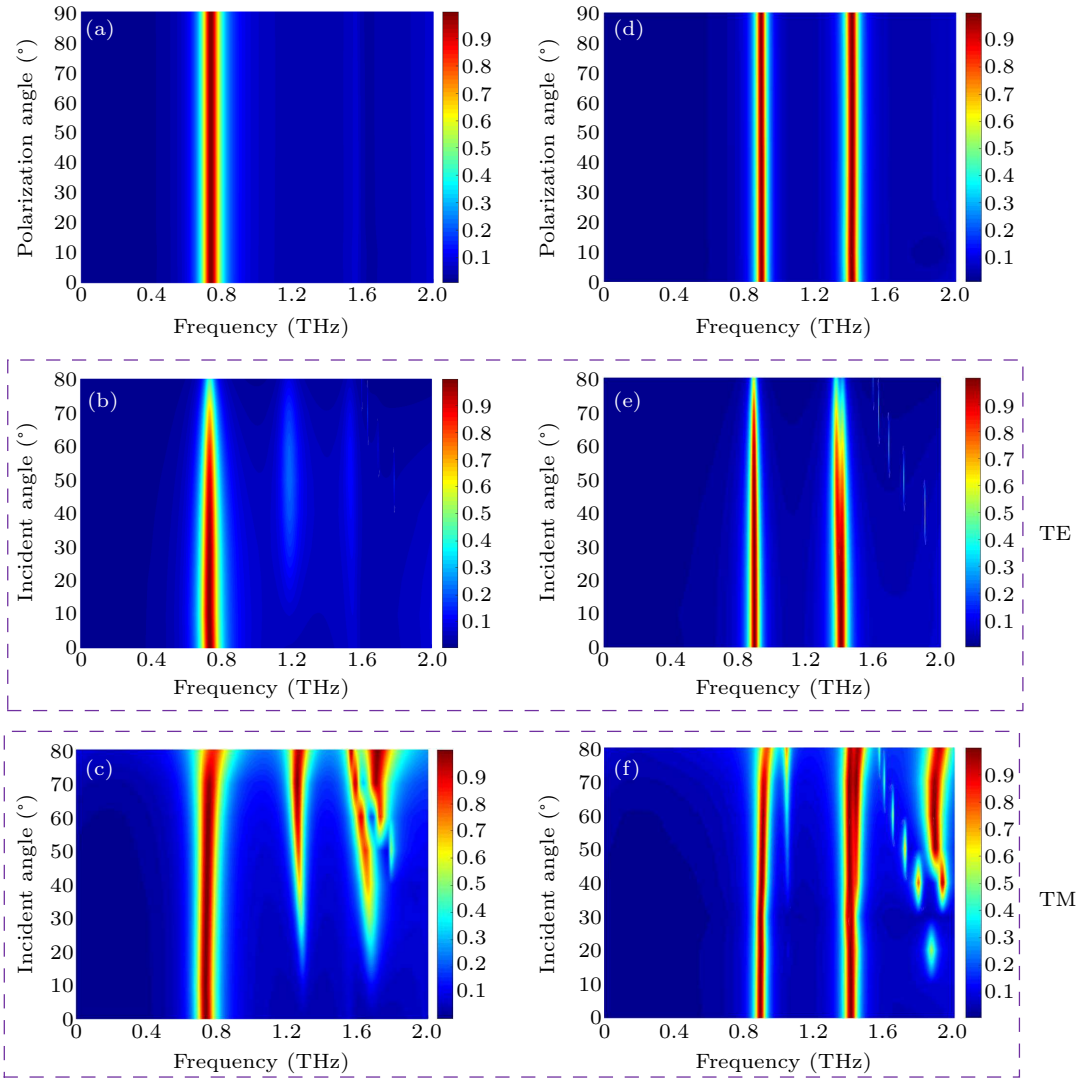


Fig. 4. Absorption spectra of single-band (a)–(c) and dual-band (d)–(f) absorbers with different polarization angles and incident angles.

3.2. Dynamic control of electromagnetically induced transparency

When both the bottom and top VO_2 patches are in an insulating state, the metasurface converts from terahertz absorption to EIT. Figure 5 depicts the transmission curves of the split rings, cross and their combination under normally incident terahertz waves when the electrochemical potential μ_c of the graphene layer is set to 0 eV. It can be concluded that the resonant peak at 1.04 THz is generated by the cross while the resonant peak at 1.58 THz is generated by the four split rings. Therefore, the bright mode induced by the four split rings and the bright mode induced by the cross produce destructive interference between adjacent resonators, which induces a transparent window in the opaque band. In order to clarify the physical mechanism of EIT, figure 6 shows the electric field distribution of the metasurface. At 1.04 THz, the cross is strongly excited by the incident terahertz wave while the four split rings are weakly excited. However, the electric field is mainly concentrated in four split rings at 1.58 THz. At a frequency of 1.24 THz, the cross and four split rings are excited at the same time, and the destructive interference caused by the hybrid coupling of the two bright modes inhibits the radiation loss and allows transmission of the incident wave.

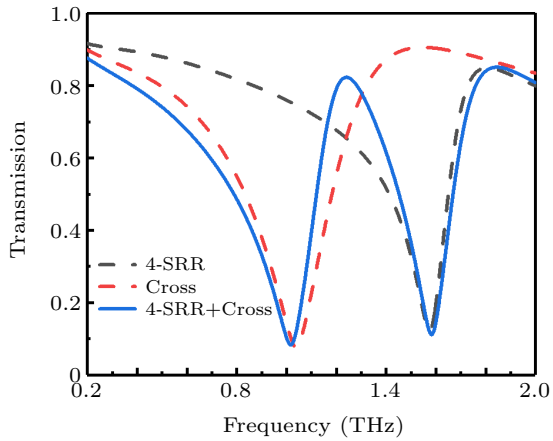


Fig. 5. Transmission curves of the split rings, cross and their combination.

The coupling mechanism of the double particle structure is employed to explain the EIT characteristics of the designed structure.[21] The cross and four split rings can be considered as particles interacting with the incident electric field, $E = E_0 e^{i\omega t}$. The coupled differential equation can be expressed as follows:[22]

$$\ddot{x}_1(t) + \gamma_1 \dot{x}_1(t) + \omega_1^2 x_1(t) + \kappa^2 x_2(t) = \frac{g_1 E}{m_1}, \tag{10}$$

$$\ddot{x}_2(t) + \gamma_2 \dot{x}_2(t) + \omega_2^2 x_2(t) + \kappa^2 x_1(t) = \frac{g_2 E}{m_2}, \tag{11}$$

where m_1 (m_2), $\dot{x}_1$ ($\dot{x}_2$), $\ddot{x}_1$ ($\ddot{x}_2$), ω_1 (ω_2), γ_1 (γ_2), and g_1 (g_2) are the effective mass, the first derivative of displacement, the second derivative of displacement, resonance frequency, loss factor and the coupling strength of the two particles with the incident terahertz wave, respectively. κ represents the coupling coefficient between the two particles. The following equations can be derived from formulae (10) and (11):

$$x_1 = \frac{\left(\frac{g_2 E}{m_2}\right) k^2 + \left(\omega^2 - \omega_2^2 + i\omega\gamma_2\right)\left(\frac{g_1 E}{m_1}\right)}{k^4 - \left(\omega^2 - \omega_1^2 + i\omega\gamma_1\right)\left(\omega^2 - \omega_2^2 + i\omega\gamma_2\right)}, \tag{12}$$

$$x_2 = \frac{\left(\frac{g_1 E}{m_1}\right) k^2 + \left(\omega^2 - \omega_1^2 + i\omega\gamma_1\right)\left(\frac{g_2 E}{m_2}\right)}{k^4 - \left(\omega^2 - \omega_1^2 + i\omega\gamma_1\right)\left(\omega^2 - \omega_2^2 + i\omega\gamma_2\right)}. \tag{13}$$

The effective polarization of the metasurface can be written as follows:

$$P = g_1 x_1 + g_2 x_2. \tag{14}$$

Assuming $A = g_1/g_2$ and $B = m_1/m_2$, the effective susceptibility χ of the EIT structure can be expressed as

$$\begin{aligned}\chi &= \frac{P}{\varepsilon_0 E} \\ &= \frac{K}{A^2 B}\left(\frac{A(B+1)k^2 + A^2\left(\omega^2 - \omega_2^2\right) + B\left(\omega^2 - \omega_1^2\right)}{k^4 - \left(\omega^2 - \omega_1^2 + i\omega\gamma_1\right)\left(\omega^2 - \omega_2^2 + i\omega\gamma_2\right)}\right) \\ &\quad + i\omega\frac{A^2\gamma_2 + B\gamma_1}{k^4 - \left(\omega^2 - \omega_1^2 + i\omega\gamma_1\right)\left(\omega^2 - \omega_2^2 + i\omega\gamma_2\right)},\end{aligned} \tag{15}$$

where K is a coefficient of proportionality. The real part of the effective susceptibility represents the dispersion characteristics and the imaginary part represents the absorption of the proposed metasurface. Figure 7 demonstrates the simulation curve and parameter fitting of the designed metasurface. The fitting parameters are $A = 0.59$, $B = 0.72$, $\kappa = 0.65$ THz, $\gamma_1 = 1.05$ rad·ps^{-1} and $\gamma_2 = 1.45$ rad·ps^{-1}. It can be observed that the calculation and simulation curves show good agreement.

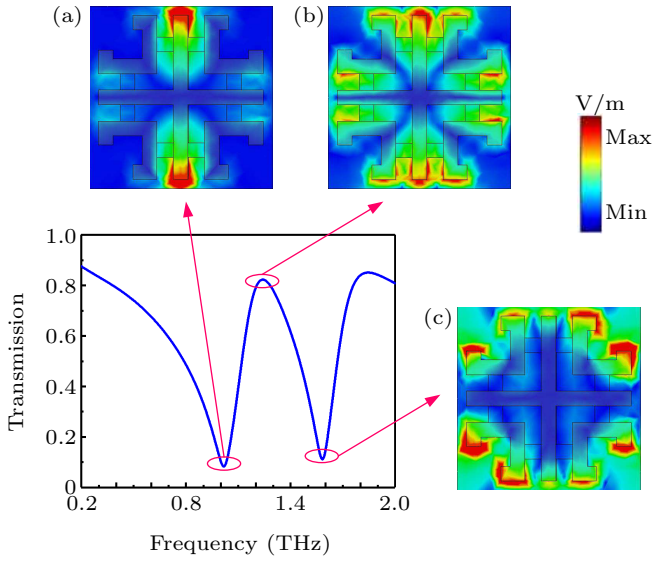


Fig. 6. Electric field distribution of the proposed metasurface: (a) 1.04 THz, (b) 1.24 THz, (c) 1.58 THz.

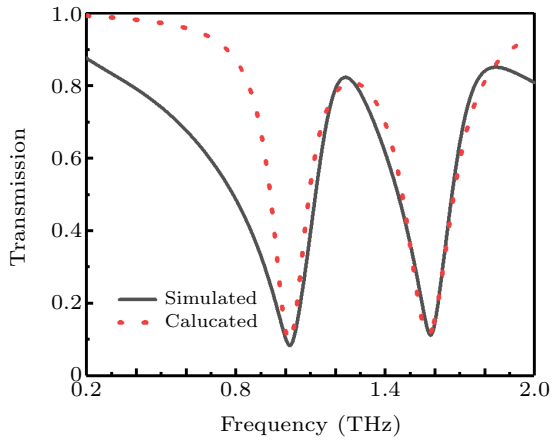


Fig. 7. Comparison of the calculated and simulated curves.

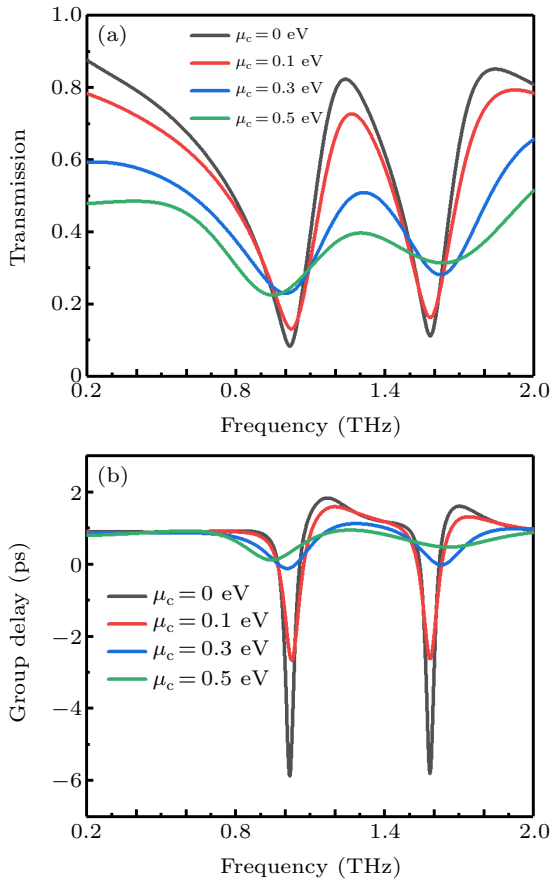


Fig. 8. Transmission curve (a) and group delay (b) of the designed metasurface for a graphene layer under different chemical potentials.

In order to realize dynamic control of the EIT phenomenon, the transmission curves of the graphene layer under different chemical potentials were calculated, as shown in Fig. 8(a). When the chemical potential of the graphene layer is 0 eV, the transmission amplitude of the designed structure is 82% at 0.24 THz. As the chemical potential of the graphene layer gradually increases from 0 eV to 0.5 eV, the transmission amplitude of the EIT peak decreases from 82% to 39%. As an important phenomenon accompanying the EIT effect, a slow light is produced by the strong dispersion of the EIT window. The group delay ($\tau_g = -\mathrm{d}\varphi/\mathrm{d}\omega$) is introduced to analyze the slow light capability of the designed metasurface. In this formula, φ and ω represent the phase shift and angular frequency, respectively, of the transmission spectrum. Since the transparent window is adjustable, active control of the group delay can also be achieved by changing the chemical potential of the graphene layer, as depicted in Fig. 8(b). When the chemical potential of the graphene layer is set as 0 eV, the maximum positive group delay is 1.83 ps at the transparent window. With an increase in the chemical potential, the device gradually loses the slow light effect, showing that active control group delay can be realized by changing the chemical potential of graphene. This has great significance for the design of slow light equipment.

4. Conclusion

In this paper, a dual-function terahertz metasurface based on VO_2 and graphene is proposed. It is composed of a gold layer embedded with VO_2 patches, a SiO_2 layer, a VO_2 layer, a graphene layer and a SiO_2 spacer substrate. When the top VO_2 patches and bottom VO_2 are in the metallic state, the designed metasurface can be used as a single-band absorber with a terahertz absorptance of 99.7% at 0.736 THz. When the top VO_2 patches are in the insulating state and the bottom VO_2 is in the metallic state, the designed metasurface behaves as a dual-band absorber, and the absorptance rates at 0.894 THz and 1.408 THz are 98.9% and 99.9%, respectively. The absorber is insensitive to polarization and maintains perfect absorption under large angles of incidence. When the bottom VO_2 layer is in the insulating state, the designed metasurface achieves electromagnetically induced transparency. When the chemical potential of graphene is varied from 0 eV to 0.5 eV, the transparent window can be dynamically regulated. Changing the chemical potential of the graphene layer can also realize active control of group delay. In summary, the designed terahertz device shows good prospects for application in tunable terahertz optoelectronic systems.

Acknowledgments

Project supported by the National Natural Science Foundation of China (Grant Nos. 61871355 and 61831012), the Talent Project of Zhejiang Provincial Department of Science and Technology (Grant No. 2018R52043), Zhejiang Key Research and Development Project of China (Grant Nos. 2021C03153 and 2022C03166), and Research Funds for the Provincial Universities of Zhejiang (Grant No. 2020YW20).

References

[1] Verleur H, Barker A and Berglund C 1968 *Phys. Rev.* **172** 788
[2] Jeong Y, Han S, Rhie J, Kyoung J, Choi J, Park N, Hong S, Kim B, Kim H and Kim H 2015 *Nano Lett.* **15** 7181
[3] Liu J and Fan L 2020 *Microw. Opt. Technol. Lett.* **62** 1681

[4] Wen Q, Zhang H, Yang Q, Xie Y, Chen K and Liu Y 2010 *Appl. Phys. Lett.* **97** 021111
[5] Liu L, Kang L, Mayer T and Werner D 2016 *Nat. Commun.* **7** 13236
[6] Li Q, Liu S, Zhang X, Wang S and Chen T 2015 *Opt. Express* **28** 8792
[7] Choi S, Kyoung J, Kim H, Park H, Park D, Kim B, Ahn Y, Rotermund F, Kim H, Ahn K and Kim D 2011 *Appl. Phys. Lett.* **98** 071105
[8] Choi H, Ahn J, Jung J, Noh T and Kim D 1996 *Phys. Rev. B* **54** 4621
[9] Liu H, Wang Z, Li L, Fan Y and Tao Z 2019 *Sci. Rep.* **9** 5751
[10] Dong X, Luo X, Zhou Y, Lu Y, Hu F, Xu X and Li G 2020 *Opt. Express* **28** 30675
[11] Deng Y and Song Z 2020 *Opt. Mater.* **105** 109972
[12] Zhang Y, Tan Y, Stormer H and Kim P 2005 *Nature* **438** 201
[13] Xiang Y, Wang L, Lin Q, Xia S, Qin M and Zhai X 2019 *IEEE Photon. Technol. Lett.* **31** 483
[14] Sun H, Zhao L, Dai J, Liang Y, Guo J, Meng H, Liu H, Dai Q and Wei Z 2020 *Nanomaterials* **10** 1359
[15] Zhu H, Zhang Y, Ye L, Li Y, Xu Y and Xu R 2020 *Opt. Express* **28** 38626
[16] Liu W, Xu J and Song J 2021 *Opt. Express* **29** 23331
[17] Wang S, Kang L and Werner D 2018 *Sci. Rep.* **8** 189
[18] Kaipa C, Yakovlev A, Hanson G, Padooru Y, Medina F and Mesa F 2012 *Phys. Rev. B* **85** 245407
[19] Gusynin V, Sharapov S and Carbotte J 2007 *J. Phys.: Condens. Matter* **19** 026222
[20] Smith D, Vier D, Koschny T and Soukoulis C 2005 *Phys. Rev. E.* **71** 036617
[21] Meng F, Wu Q, Erni D, Wu K and Lee J 2012 *IEEE Trans. Microw. Theory Tech.* **60** 3013
[22] Ma. Y, Li Z, Yang Y, Huang R, Singh R, Zhang S, Gu J, Tian Z, Han J and Zhang W 2011 *Opt. Mater. Express* **1** 391